

Quantitative Analysis of Scanning Tunneling Microscopy Images of Mixed-Ligand-Functionalized Nanoparticles

Fabio Biscarini,^{*,†} Quy Khac Ong,[‡] Cristiano Albonetti,[§] Fabiola Liscio,^{||} Maria Longobardi,[⊥] Kunal S. Mali,[#] Artur Ciesielski,[○] Javier Reguera,[‡] Christoph Renner,[⊥] Steven De Feyter,[#] Paolo Samori,[○] and Francesco Stellacci[‡]

[†]Dip. Scienze della Vita, Università di Modena e Reggio Emilia, Via Campi 183, 41125 Modena, Italy

[‡]Institute of Materials, École Polytechnique Fédérale de Lausanne, Lausanne, Switzerland

[§]Consiglio Nazionale delle Ricerche, Istituto per lo Studio dei Materiali Nanostrutturati (CNR-ISMN), Via P. Gobetti 101, I-40129 Bologna, Italy

^{||}Consiglio Nazionale delle Ricerche, Istituto di Microelettronica e Microsistemi (CNR-IMM), Via P. Gobetti 101, I-40129 Bologna, Italy

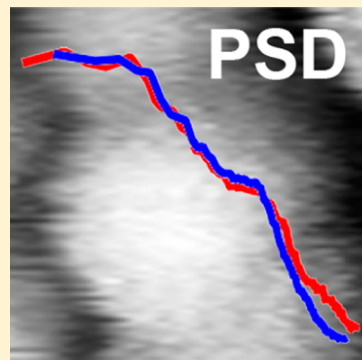
[⊥]Department of Condensed Matter Physics, NCCR Materials with Novel Electronic Properties, University of Geneva, 24 Quai Ernest-Ansermet, CH-1211 Geneva 4, Switzerland

[#]Department of Chemistry, Division of Molecular Imaging and Photonics, KU Leuven - University of Leuven, Celestijnenlaan 200F, 3001 Leuven, Belgium

[○]Laboratoire de Nanochimie, ISIS & icFRC, Université de Strasbourg & CNRS, 8 allée Gaspard Monge, 67000 Strasbourg, France

Supporting Information

ABSTRACT: Ligand-protected gold nanoparticles exhibit large local curvatures, features rapidly varying over small scales, and chemical heterogeneity. Their imaging by scanning tunneling microscopy (STM) can, in principle, provide direct information on the architecture of their ligand shell, yet STM images require laborious analysis and are challenging to interpret. Here, we report a straightforward, robust, and rigorous method for the quantitative analysis of the multiscale features contained in STM images of samples consisting of functionalized Au nanoparticles deposited onto Au/mica. The method relies on the analysis of the topographical power spectral density (PSD) and allows us to extract the characteristic length scales of the features exhibited by nanoparticles in STM images. For the mixed-ligand-protected Au nanoparticles analyzed here, the characteristic length scale is 1.2 ± 0.1 nm, whereas for the homoligand Au NPs this scale is 0.75 ± 0.05 nm. These length scales represent spatial correlations independent of scanning parameters, and hence the features in the PSD can be ascribed to a fingerprint of the STM contrast of ligand-protected nanoparticles. PSD spectra from images recorded at different laboratories using different microscopes and operators can be overlapped across most of the frequency range, proving that the features in the STM images of nanoparticles can be compared and reproduced.



Noble metal nanomaterials, and specifically gold nanoparticles (NPs), have attracted considerable attention because of their potential applications in technological fields ranging from electronics to optics to catalysis to medicine.^{1–7} Among the most investigated forms of gold nanoparticles, those with monolayer coatings are particularly attractive. The self-assembled monolayer (SAM) that protects the particles (hereafter called ligand shell) is used to impart some of the key NP properties needed. For instance, in nanomedicine, the ligand shell contains the key components needed for drug delivery or target recognition.⁸ Various techniques can be applied to characterize the ligand shell including electron spin resonance,^{9–14} nuclear magnetic resonance,^{15–20} infrared spectroscopy,^{21,22} differential scanning calorimetry,^{23,24} thermal gravimetric analysis,²¹ transmission electron microscopy,^{25–27}

and scanning probe microscopy.^{28–30} However, a full characterization of the ligand shell in terms of composition, compositional variation, density, structure, and morphology remains a major challenge because there is no single technique that is able to provide information on all of these properties at the same time.

In these NPs, the gold core is protected by a SAM of thiolated molecules whose properties can be related to those of SAMs on flat surfaces. Weiss and co-workers showed by scanning tunneling microscopy (STM) imaging that on flat Au(111) surfaces SAMs composed of binary mixtures of

Received: September 16, 2013

Revised: September 30, 2013

Published: October 2, 2013

different molecules (i.e., molecules with a driving force for demixing as discussed in ref 31) undergo spontaneous phase segregation into domains of varying size and shape.^{32–34} Stellacci and co-workers reported that similar SAMs of different molecules assembled on ~5-nm-diameter Au NPs cores, exhibit a spatial modulation of the STM topography.^{29,35} The existence of such spatially modulated architecture, termed stripe-like domains, was recently supported by high-resolution STM images that show the molecules that compose these single domains³⁶ as well as high-resolution atomic force microscopy images.³⁰ The presence of these stripe-like domains has been supported by neutron diffraction,³⁷ infrared spectroscopy,²² nuclear magnetic resonance,¹⁵ and predicted by various types of simulations.^{31,38,39} Glotzer and co-workers explained the phenomenon as being due to the balance between the enthalpy of phase segregation and the interfacial conformational entropy that is established when long molecules form a domain boundary with shorter ones.³¹

STM images remain as key evidence for the existence of stripe-like domains on Au NPs coated with binary mixtures of ligand molecules. Through the years, many images have been acquired and analyzed in a series of papers.^{29,35,40} Striations whose width varies in a relatively narrow range centered around 1 nm were observed on mixed-ligand NPs. In a separate publication,³⁶ it has been shown that high-resolution images can be acquired, where the single molecules that compose the stripe-like domains are imaged. The possibility to acquire images with features similar to the striations present on the nanoparticle due, instead, to feedback loop artifacts was pointed out in 2004²⁹ and then extensively discussed in follow-up papers.^{35,40} It was established that whereas the width of the artifact features scales linearly with tip speed and is independent of the chemical composition of the imaged sample, features on NPs are conserved across imaging parameters, varying only when the chemical nature of the imaged particles changes. However, these conclusions were reached through manual measurements of peak distances across line scans.²⁵ Because of the method and the complexity of these specific samples (that present features on various length scales, all with a sizable distribution in length), confidence in the reliability of the manual measurements requires the construction of a large statistical set by independent operators to guarantee the absence of a bias.^{35,40} A robust operator-independent analysis of the STM images of these NPs has not been reported to date.

Here, we propose power spectral density (PSD) analysis as an effective operator-independent method of extracting information from STM images of nanoparticles. PSD is the norm squared of the Fourier transform of the STM topography and represents the contributions of the different spatial length scales to the topography fluctuations. Its definition is given in the Experimental and Methods Section. Given a topographical image with N points along each line scan whose length is L , the spatial frequencies f (with f being the inverse of a length scale) sampled in the STM image range from the inverse scan length $1/L$ up to the Nyquist frequency $N/2L$.^{41–43} PSD exploits the whole information content present in the image, as opposed to the analysis of manually drawn line profiles in real space. It has been shown that the PSD from scanning probe microscopy images provides valuable information on samples whose complex morphology is not straightforward to analyze in real space because of superposition, entanglement, or coalescence of features. Successful applications of PSD analyses include the identification of morphological transitions in organic and

polymeric thin films,⁴⁴ the extraction of morphological parameters from images of porous networks of entangled biomolecules,⁴⁵ correlations of morphological parameters with device properties,⁴⁶ and a comparison of forensic samples.⁴⁷ PSD analysis is also useful for comparing information from different techniques probing different ranges of spatial lengths scales.^{42,48–50}

In this article, we show that PSD readily displays the multiscale features present in the STM images: NP size, interparticle distance, and the characteristic length scale on the particles. PSD analysis allowed us to show that STM images recorded in four different laboratories with different microscopes and different imaging parameters are essentially equivalent over a broad range of spatial frequencies. We also show that the information contained in high- and low-resolution images arises from the same features on the nanoparticles. Our interpretation of the PSD features is validated by the comparison with those obtained from artificially generated images.

RESULTS

Figure 1a is an STM image acquired in 2004 at MIT of 2:1 1-octanethiol (OT)/mercaptopropionic acid (MPA) nanoparticles. In Figure 1b–f, we report representative STM images that were recorded in different laboratories on the same sample

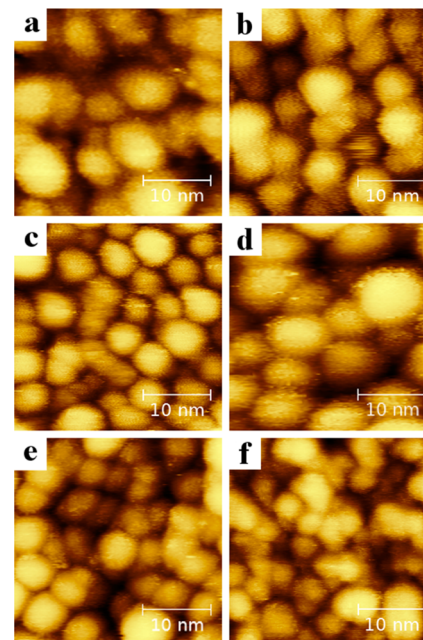


Figure 1. STM topographical images of mixed-ligand-protected NPs acquired at different locations and times: (a) OT/MPA 2:1 sample, MIT, scan length $L = 49.0$ nm, image size IS = 30.1 nm, bias voltage $V_b = 1100$ mV, set-point tunneling current $I_t = 0.63$ nA, scan rate $\nu = 5.1$ Hz, year 2003. Images of C11ol/C4ol 1:1 NPs in the same sample acquired at (b) EPFL $L = 30.0$ nm, IS = 30.0 nm, $V_b = 700$ mV, $I_t = 0.1$ nA, $\nu = 20.3$ Hz, year 2012. (c) UG $L = 50.0$ nm, IS = 30.1 nm, $V_b = -200$ mV, $I_t = 2$ nA, $\nu = 1.9$ Hz, year 2013. (d) UdS $L = 80.0$ nm, IS = 30.1 nm, $V_b = 200$ mV, $I_t = 0.02$ nA, $\nu = 7.6$ Hz, year 2013. (e) KUL using a Bruker, $L = 71.4$ nm, IS = 30.0 nm, $V_b = 700$ mV, $I_t = 0.05$ nA, $\nu = 6.1$ Hz, year 2013. (f) KUL using an Agilent, $L = 50.0$ nm, IS = 30.0 nm, $V_b = -500$ mV, $I_t = 0.03$ nA, $\nu = 4.8$ Hz, year 2013. All images were acquired at 512 pixels \times 512 pixels with the exception of the EPFL that was acquired at 256 pixels \times 256 pixels. The color scale is oversaturated to highlight the features on the NPs.

of 1:1 11-mercaptopropanoic acid (C11ol)/4-mercaptopropanoic acid (C4ol) NPs. The images show NPs forming a noncompact film, with their apparent NP diameter amounting to 9.4 ± 2.6 nm, as determined from valley-to-valley measurements on line profiles in the STM images. The Au NP core has a diameter of 3.9 ± 1.1 nm, as estimated from transmission electron microscopy, and the fully stretched length of the C11ol ligand is ~ 1.5 nm, leading to a total expected diameter of 6.9 nm. The difference between the expected number and the measured one is due to the effect of the tip envelope, maximized by the fact that, for consistency reasons, in STM the particle size was measured as the valley-to-valley distance in line profiles.⁵¹ The STM contrast on top of NPs exhibits superimposed features that contribute additional fluctuations to the topography. On NPs, a few seemingly periodic fluctuations can be detected; however, it is difficult to assess unambiguously the occurrence of a truly periodic structure. These fluctuations are present on a number of NPs on most of the images acquired at different laboratories. Although all of the images contain NPs with similar features on them, they also present differences. Hence it is difficult to assess objectively by visual inspection whether the images have been reproduced across laboratories.

In Figure 2, we compare the PSDs vs k , displayed as a double-log plot, obtained from each image in Figure 1b–f. From Figure 2a, it is evident that the PSDs exhibit similar features, with some differences. For the discussion, we have marked in the plot the features with the corresponding Roman numerals and delimited their range with vertical black lines: (i) a plateau (white spectrum) at low frequency, whose lower limit is due to the scan length encompassing the characteristic size of several NPs, followed by a smoothly varying elbow; (ii) a steep decay, resembling a power law $k^{-\gamma}$ with exponent $\gamma > 1$, starting from about $k = 0.6 \times 10^9$ m⁻¹ (corresponding to a 10 nm length scale l) down to about 3×10^9 m⁻¹ (corresponding to $l \approx 2$ nm); (iii) either a shoulder or a broad peak in the range from $3.3(\pm 0.4) \times 10^9$ m⁻¹ ($l = 1.9 \pm 0.2$ nm) to $5.9(\pm 0.3) \times 10^9$ m⁻¹ ($l = 1.07 \pm 0.05$ nm); (iv) for the PSDs of images acquired at RT, a steep decay from 6.2×10^9 m⁻¹ to above 1.0×10^{10} m⁻¹ ($l < 0.6$ nm). In a few instances, as for the image acquired in UHV at low temperature, there is a broad peak followed by a steep decay in the same range. (The values provided for the boundaries of the features were estimated as intersections between one feature and the next. They are given with errors because they are averaged over several PSD curves. The boundaries are drawn as continuous black vertical lines in Figure 2.) A similar trend is also observed in the PSD of KUL acquired with an Agilent microscope, although we have fewer images to assess the statistical occurrence of this observation. Significantly, these features (i–iv) are conserved in all PSDs of mixed-ligand NPs. All of the RT measurements show a clear feature (iii): it appears as a broad peak in the EPFL image and as a shoulder in the UdS and KUL images. At 77 K (UG), features (iii) and (iv) merge into a broader peak. This implies that the UG image also exhibits features whose correlation length is ~ 0.5 nm. This may be due to better imaging conditions or to lower imaging temperature. Figure 2a shows how images of mixed-ligand NPs recorded in different laboratories under different conditions with different operators, instruments, and time all exhibit feature (iii).

To extract the characteristic length scales of the PSDs, we have devised a phenomenological functional to fit each PSD across the whole frequency domain. The fitting functional is a

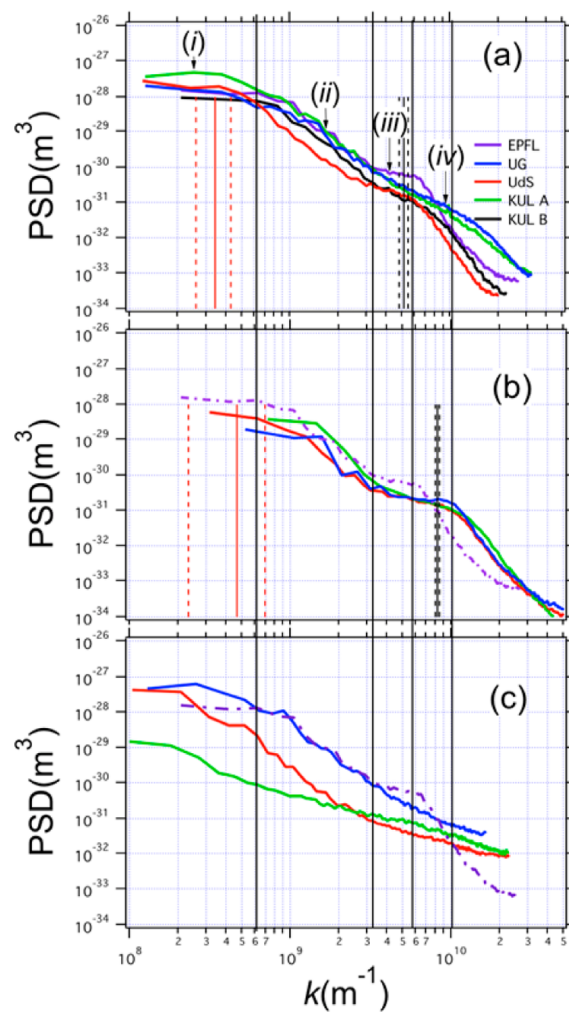


Figure 2. (a) PSDs vs wave vector k for the STM images in Figure 1b–f. PSDs were evaluated at $M = N/2$ frequencies: EPFL, $M = 128$; UG, $M = 256$; UdS, $M = 167$; KUL Agilent, $M = 256$; and KUL Bruker, $M = 108$. The zero-frequency contribution has been removed. The color code and the symbols correspond to the laboratories where the image was acquired. The features described in the text are tagged with Roman numerals and delimited by vertical solid, black lines at the mean values quoted in the text. The vertical segments represent the values of $\langle k_{c1} \rangle$ and $\langle k_{c2} \rangle$ (solid) and their values ± 1 SEM (dashes). (b) PSDs of homologand C11ol NPs (red) with scan length $L = 20$ nm, image size IS = 20 nm, bias voltage $V_b = 800$ mV, set-point tunneling current $I_t = 0.1$ nA, scan rate $\nu = 15.2$ Hz, year 2013; (green) $L = 8.7$ nm, IS = 8.7 nm, $V_b = 600$ mV, $I_t = 0.2$ nA, $\nu = 30.5$ Hz, year 2013; and (blue) $L = 12$ nm, IS = 12 nm, $V_b = 300$ mV, $I_t = 0.1$ nA, $\nu = 30.5$ Hz, year 2013. The vertical segments represent the values of $\langle k_{c1} \rangle$ and $\langle k_{c2} \rangle$ (solid) and their values ± 1 SEM (dashes). (c) PSD of control samples: (red) Au film on glass $L = 70$ nm, IS = 70 nm, $V_b = 50$ mV, $I_t = 0.3$ nA, $\nu = 1$ Hz, year 2013; (green) Au film on mica $L = 70$ nm, IS = 70 nm, $V_b = 50$ mV, $I_t = 0.5$ nA, $\nu = 1$ Hz, year 2013; (blue) C11ol/C4ol NP image with no features on the NPs $L = 48.6$ nm, IS = 48.6 nm, $V_b = 500$ mV, $I_t = 0.5$ nA, $\nu = 2$ Hz, year 2013. Dotted-dashed curves in b and c represent the EPFL PSD from a, used as comparison.

linear combination of two stretched exponentials together with a $1/f$ noise contribution. It reads as

$$\text{PSD}(k) = A_1 \exp\left[-\left(\frac{k}{k_{c1}}\right)^{\gamma_1}\right] + A_2 \exp\left[-\left(\frac{k}{k_{c2}}\right)^{\gamma_2}\right] + \frac{A_3}{k} \quad (1)$$

The functional eq 1 has seven parameters. We saturate A_1 and A_2 with the mean values of the plateau in region I and feature (iii), and we fix A_3 at a value that best reproduces the highest-frequency part (typically 10^{-23} – 10^{-24} m³). We then best fit each PSD in Figure 2a using just four parameters, namely, wave vectors k_{c1} and k_{c2} and exponents γ_1 and γ_2 of the stretched exponentials. Wave vectors k_{c1} and k_{c2} are related to the characteristic length scales (correlation lengths) ξ_1 and ξ_2 by $k_{cn} = 2\pi/\xi_n$, with $n = 1, 2$. These are the length scales associated with feature (i) and feature (iii), respectively.

In Figure S1a, we show the results of the fitting of the PSDs in Figure 2a. The fitting curves closely overlap the experimental PSDs. The fitting parameters are shown in Figure S2; they are extracted from PSDs of images acquired at different laboratories and are effectively invariant. The mean values (viz. averaged across the values of the laboratories) of k_{c1} and k_{c2} , together with their errors estimated as standard error of the mean (SEM), and the corresponding values of ξ_1 and ξ_2 , together with their errors $\Delta\xi$ evaluated by propagation, are reported in Table 1. The characteristic length scale ξ_2 associated with

Table 1. Results of the Fitting According to Equation 1

figure	$\langle k_{c1} \rangle$ (m ⁻¹)	SEM(k_{c1}) (m ⁻¹)	$\langle k_{c2} \rangle$ (m ⁻¹)	SEM(k_{c2}) (m ⁻¹)
2a	3.43×10^8	8.4×10^7	5.14×10^9	3.2×10^8
2b	4.7×10^8	2.3×10^8	8.3×10^9	6.0×10^8
3a	N/A	N/A	5.91×10^9	7.5×10^8
figure	ξ_1 (nm)	$\Delta\xi_1$ (nm)	ξ_2 (nm)	$\Delta\xi_2$ (nm)
2a	18.3	4.5	1.22	0.08
2b	13.5	6.7	0.76	0.05
3a	N/A	N/A	1.06	0.13

feature (iii) takes a value of 1.22 ± 0.08 nm. Mean values $\langle k_{c1} \rangle$ and $\langle k_{c2} \rangle$ are also graphically shown in Figure 2a as red and black vertical segments, respectively.

In Figure 2b, we compare the PSDs (continuous lines) from images of homoligand C11ol NPs with a PSD of mixed-ligand 1:1 C11ol/C4ol NPs (EPFL from Figure 2a, dashed line). We notice that all PSDs of homoligand NPs show the peak broadened in the range of features (iii) and (iv). The fitting with eq 1 yields the parameters reported in Table 1. Mean values $\langle k_{c1} \rangle$ and $\langle k_{c2} \rangle$ are graphically overlaid in Figure 2b. Importantly, ξ_2 shifts from 1.22 ± 0.08 nm for mixed-ligand NPs to 0.76 ± 0.05 nm for homoligand NPs.

Figure 2c shows that images of (a) gold on mica, (b) gold hemispheres on silicon, and (c) featureless gold nanoparticles all lack feature (iii). Figure S3 in the Supporting Information shows that the PSD of images taken with a fixed tip (scan length 0 nm) in the four locations all lack feature (iii).

We used PSD not only to analyze images of C11ol/C4ol NP but also to analyze images of the 2:1 OT/MPA originally reported and the object of extensive studies.^{35,40} Figure 1a shows an STM image of these NPs taken in 2004. A comparison of PSDs that were obtained from images recorded under various conditions at MIT is shown in Figure 3a. It is evident how the best-fit values of k_{c2} (colored vertical segments in Figure 3a) within the wave vector range of feature (iii) from $3.2(\pm 0.6) \times 10^9$ m⁻¹ ($l = 1.9 \pm 0.3$ nm) to $6.7(\pm 1.4) \times 10^9$ m⁻¹ ($l = 0.9 \pm 0.2$ nm). We notice that feature (iii) varies in shape as a reflection of the image quality by analogy to the features exhibited in Figure 2a. The characteristic length scale is found to be 1.06 ± 0.13 nm (Table 1).

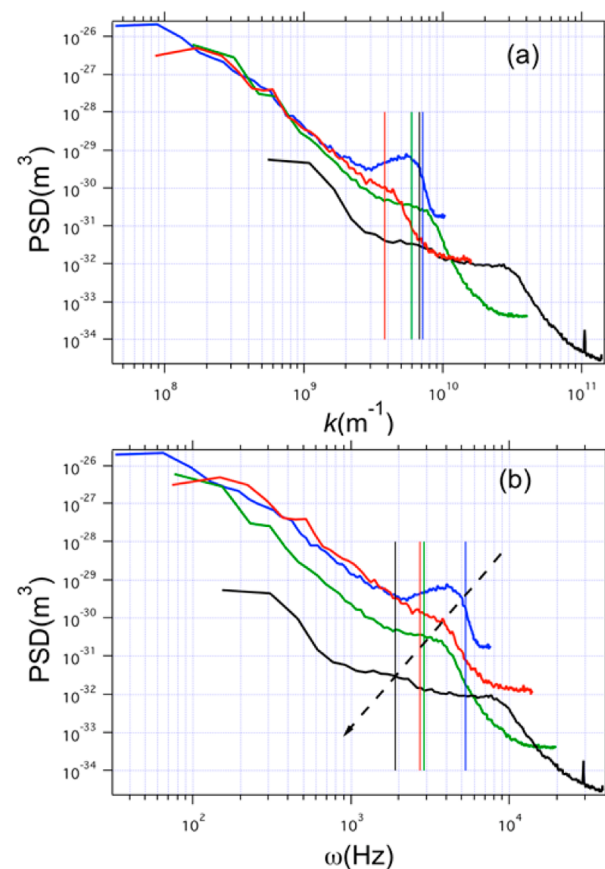


Figure 3. (a) PSDs vs wave vector k for a series of STM images of OT/MPA 2:1 NPs acquired at MIT in 2004. Scan rate ν , scan length L , and number of sampled frequencies $M = \frac{N}{2}$ are indicated: (blue) $\nu = 2.35$ Hz, $L = 157$ nm, $M = 234$; (red) $\nu = 4.36$ Hz, $L = 100$ nm, $M = 190$; (green) $\nu = 6.1$ Hz, $L = 40$ nm, $M = 256$; and (black) $\nu = 12.21$ Hz, $L = 11.5$ nm, $M = 256$. The vertical segment of the same color indicates the value of k_{c2} from the best fit of the PSD. (b) Rescaled PSD vs time frequency of the same plots shown in b. The dashed arrow is a guide to the eye connecting the PSD values at rescaled k_{c2} with the exception of the red PSD (that is off-trend). All images analyzed here were analyzed in refs 29 and 40.

To discriminate between spatial versus time-dependent features, in Figure 3b we rescale the PSD plots shown in Figure 3a upon changing the horizontal scale from spatial wave vector k to a time frequency ω according to the equation

$$\omega = v \cdot k = n \cdot L \cdot \nu \cdot k \quad (2)$$

Again, L is the scan length of the image (in meters), ν is the STM scan rate in Hz, and n is an instrumental factor that depends on the way the microscope relates the tip linear speed v to the scan rate ν . n is 1 for Omicron and Agilent microscopes and 2 for Bruker microscopes. It is evident from Figure 3b that k_{c2} is “offset” in the time-frequency domain in the case of the NP images that were deemed genuine. The red PSD appears off-trend, thus its image might be contaminated by instrumental noise. Figure S4 in the Supporting Information shows that a similar offset is observed when rescaling the PSD spectra shown in Figure 2a,b.

Figure 4a shows a representative STM image of a 2:1 OT/MPA-coated granular Au film on Si. Also, this image is a part of the images recorded in 2004.²⁹ Here, grains are larger than the NPs (curvature radius of about 20 nm, to be compared to ~ 5 nm of the NPs in Figure 1a). The STM image shows periodic

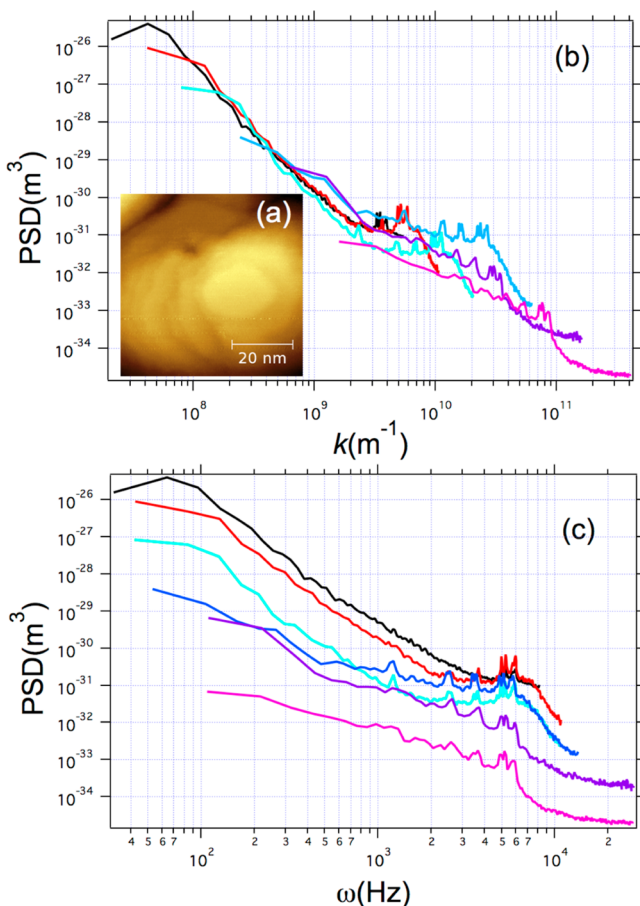


Figure 4. (a) STM topography image of Au grains on Si coated with a 2:1 mixture of OT/MPA acquired in 2004. Feedback loop oscillations are superimposed on the topographical corrugation. (b) PSDs vs wave vector of a series of STM images of the sample shown in image a. Scan rate ν , lengths L , and number of sampled frequencies $M = \frac{N}{2}$ are indicated: (black) $\nu = 2.543$ Hz, $L = 300$ nm; (red) $\nu = 3.391$ Hz, $L = 151$ nm; (green) $\nu = 3.391$ Hz, $L = 78$ nm; (light blue) $\nu = 3.391$ Hz, $L = 78$ nm; (blue) $\nu = 4.36$ Hz, $L = 25$ nm; (purple) $\nu = 8.719$ Hz, $L = 10$ nm; and (pink) $\nu = 8.719$ Hz, $L = 3.9$ nm. (c) Rescaled PSD vs time frequency of the same plots shown in image b. All images analyzed here were reported in refs 29 and 40. The zero-frequency point has been removed from each line in images b and c.

noise that was generated by an excessive gain in the feedback loop. The corresponding PSDs exhibit different features with respect to what was discussed in Figure 3b. First, for the images with the smallest scan lengths that are comparable to or smaller than the grain size, plateau feature (i) is absent. Second, feature (iii) occurs at different spatial frequencies (Figure 4b). Upon applying the rescaling (eq 2) from spatial to time frequencies, we find that the features in the PSD of noisy images (Figure 4c) align perfectly, consistent with their origin due to feedback ringing. The same rescaling (eq 2) applied to both the PSDs from the most recent data set with 1:1 C4ol/C11ol NPs (Figure S4a) and to the homoligand C11ol NPs (Figure S4b) leads to the offset of feature (iii) similar to what is shown in Figure 3c. We infer that feature (iii) in Figures 2a,b and 3b and feature iv in the image of homoligand nanoparticles in Figure 2b have a genuine spatial origin and are not generated by periodic instrumental noise.

In Figure 5a, we show a high-resolution STM image of a 1:1 C4ol/C11ol NP at a scan length comparable to the size of a

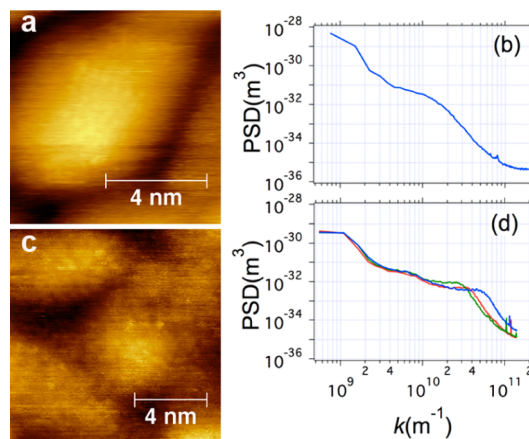


Figure 5. (a) STM topography image of a single C11ol/C4ol NP. The dots visible on the particle are the headgroups of one of the two molecules in the ligand shell of the particle. The arrows indicate three rows of aligned dots. The headgroups have a characteristic spacing, and the rows show roughly twice such spacing. The image is taken from ref 36, where it has been analyzed and described in depth together with similar images. (b) PSD of the image in part a. (c) High-resolution STM image of 2:1 OT/MPA NPs recorded in 2008 (and analyzed in ref 40) at $V_b = 200$ mV and $I_t = 0.05$ nA. (d) PSDs of the image shown in part c and of two other images of the same particles recorded at different speeds. PSDs have been evaluated at 256 frequencies.

single NP. A modulation of the signal on the NPs is observed, as contributed by circular dots closer to one another along stripe-like domains and further apart on adjacent stripes. This image, along with other images of comparable resolution, is discussed in a recent paper.³⁶ The PSD in Figure 5b exhibits a first (smaller) peak that goes from 1.4 to 0.8 nm, followed by a broad peak within an ~0.5 nm region. The similarity between this PSD and that from UG shown in Figure 2a is evident and further confirm the interpretation we give of the latter. A high-resolution image of OT/MPA 2:1 nanoparticles is shown in Figure 5c. In Figure 5d, three PSDs (one from Figure 3c, the other two from images of the same particles acquired at different tip velocity) exhibit distinct peak-like feature (iii). We notice that the PSD decay following features (iii) and (iv) depends on the scanning conditions, whereas feature (iii) does not. This is illustrated in Figure S5, where the rescaled plots according to eq 2 show the collapsing of the decaying high-frequency tail and the simultaneous offset of peak-like feature (iii).

PSD analysis allows one to compare images acquired at different length scales in different regions of the sample. Figure 6 shows the superposition (“stitching”) of the spectra from images acquired at different scan lengths varying across more than 1 order of magnitude of length scale. High-resolution images contain a wealth of details on the structure of the ligand shell on a single particle but lack a statistical information being composed of only a few NPs. Lower resolution images show fewer details on the NPs but are composed of a larger sample of NPs. The possibility to stitch the PSDs of these images allows us to propagate the molecular-scale information in the high-resolution images onto a larger sample set. PSDs can therefore be used to treat high- and low-resolution images on the same footing. The deviations from the overlapping trends in the high-frequency tails of each PSD are not relevant because we have assessed empirically that this is affected by the choice of the

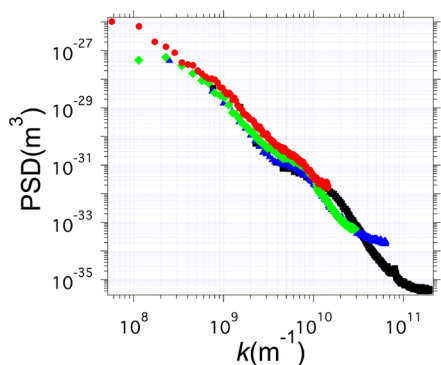


Figure 6. Stitching of PSDs of STM images of C11ol/C4ol acquired on the same sample at different length scales, indicated by different colors: $L = 8.25 \text{ nm}$ (black markers), 25.2 nm (blue), 55.2 nm (green), and 110 nm (red). PSDs have been evaluated at 256 frequencies.

windowing function in the PSD estimated by FFT. In the PSDs shown throughout the article, the default Hanning windowing in Gwyddion has been used.

To assess our interpretation of the PSD of the particles, we generated two sets of “artificial” images and analyzed them in the same way that we analyzed the experimental STM images. The first set of artificial images was generated in order to resemble closely an ideal image produced by an STM tip perfectly tracking a set of striped particles on a surface. We started with a series of hemispheres on a surface; the image was $512 \text{ pixels} \times 512 \text{ pixels}$ and was assumed to represent an area of $50 \times 50 \text{ nm}^2$, being a typical scan size for the images that we acquired. The areal density of the particles and their size distribution (log-normal, median diameter $d = 6 \text{ nm}$, shape parameter $\sigma = 0.2$) were chosen to yield an image resembling those that we typically acquire. On these particles, we overlapped idealized stripes chosen so that the stripe spacing at the particle center was 1 nm and the spacing of the stripes would diminish gradually from the center to the edges. The matching of the line profiles from the artificial image with a scan line extracted from an experimental STM image is evidenced in Figure 7b. Figure 7c shows a comparison between the PSD of an experimental image to that of an artificial image. The striking resemblance validates our interpretation of the PSD. In particular, the PSD (not shown) of images of particles with no stripes lack feature (iii), even when white or pink ($1/f$) noise is superimposed on it. Feature (iii) appears when stripes are added to the particles: it is sharp when the stripes are aligned and becomes broader only when significant misalignment is added (as shown in Figure 7a). When aligned stripes of varying width are introduced, several distinct peaks appear in the PSD, and only when misalignment is introduced do the peaks coalesce into a single broad feature (iii). We infer that broad feature (iii) in the experimental PSD arises from stripe-like domains that vary in size, spacing, and alignment across our sample. We notice that the highest spatial frequency that delimits feature (iii) in the PSDs of these artificial images closely matches the periodicity drawn on the nanoparticles. If the periodicity lies at an angle with respect to the horizontal axis, then it will be detected on a longer length scale. We infer that the periodicity present on the nanoparticles should be associated with the lower value of the characteristic length scale that can be extracted in the 1D PSD along the horizontal scan direction. We conclude that the highest frequency present in feature (iii) corresponds to the characteristic length scale truly

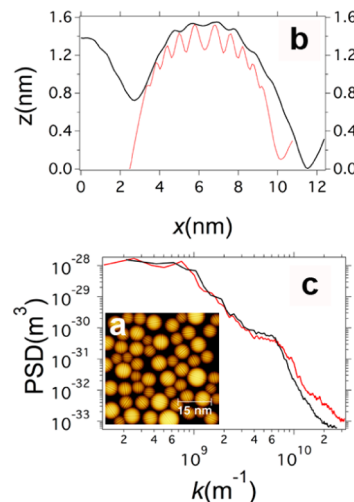


Figure 7. (a) Artificial image of a polydisperse sample of nanoparticles with randomly oriented stripes superimposed. The stripe width decreases on going from the center of the particle to the edges. (b) Cross section of a particle in the image compared to an experimental line scan. The particle size has been rescaled to be closer to the experimental profile. (c) Comparison of the PSD of the simulated image and of the experimental PSD (tagged EPFL in Figure 2a).

present on the NPs. In the framework of our fitting function (eq 1), ξ_2 should be identified as the best estimate of this characteristic length scale. We noticed that the precise value of the characteristic length scale is affected by the choice of the windowing function, thus suggesting leakage from the higher frequencies closer to the Nyquist frequency and consequently correlated with scan length L .

Another key observation is that images generated by feedback loop oscillations are similar to genuine images of striped particles but have features that scale with the tip speed, proportional to the scan rate. To validate this observation we used one of our artificial images of NP. We selected the image that had only hemispheres with no features on them. We then simulated the STM images produced according to known simplified models for STM feedback.⁵² We used parameters to simulate high gain and hence generated images containing feedback loop oscillations. A representative artificial image is shown in Figure 8a and can be compared to an experimental image with excess gain (Figure 8c). Both in the simulation and in the experiments we kept all of the parameters the same and generated images at different tip speeds. In Figure 8b, d, we show the dependence of the PSD on the acquisition speed in simulated and experimental images, respectively. The PSDs exhibit a marked peak that shifts toward higher frequencies as the tip speed is decreased. As shown in Figures 3 and 4, feature (iii) is offset when the PSD of genuine images containing feature (iii) in the same spatial frequency range are rescaled in the temporal frequency range. The opposite happens to PSD features of images that are dominated by noise. In the latter case, all of the features align and overlap substantially when plotted in the time domain. In Figure 8c, f, this behavior is highlighted, showing a remarkable alignment of the features when plotted in the time domain. The similarity between simulation and experimental data validates our interpretation.

Finally, to address the interplay between scanning probe imaging and the perceived alignment of the features on the nanoparticles with the slow scan axis we produced an image (shown in Figure 9a) of $1/f$ noise typical in STM images

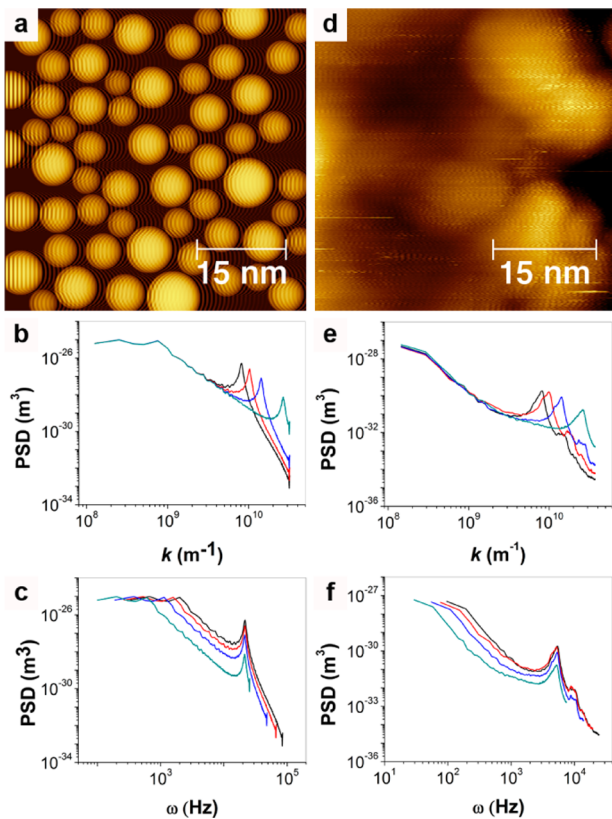


Figure 8. (a) Simulated image of a nanoparticle sample with feedback loop oscillations due to high gain and speed in imaging. (b) PSDs of the simulated images at different tip speeds: (black) $5.3 \mu\text{m/s}$, (red) $4.2 \mu\text{m/s}$, (blue) $3 \mu\text{m/s}$, and (green) $1.6 \mu\text{m/s}$. (c) PSDs for image b vs rescaled temporal frequency. (d) STM image of Au NPs exhibiting feedback loop oscillations. (e) PSD of four images acquired at different tip speeds: (black) $1.32 \mu\text{m/s}$, (red) $1.05 \mu\text{m/s}$, (blue) $0.75 \mu\text{m/s}$, and (green) $0.40 \mu\text{m/s}$. (f) PSDs for image e vs the rescaled temporal frequency.

according to the procedure described in ref 53. The horizontal and vertical PSDs of the image are shown in Figure 9b. In scanning probe images, the noise level is higher along the slow-scan axis.^{42,54} This is evident when comparing the two PSD plots. Figure 9c depicts the same image shown in Figure 7a with its vertical and horizontal PSDs plotted in Figure 9d. The overlap between the two PSDs confirms the isotropy of this image. Figure 9e is the sum of the $1/f$ noise image (Figure 9a) with the particle image (Figure 9c). It is noticeable how the effect of the $1/f$ noise is to blur the horizontal features that almost disappear visually. Conversely, there is almost no noticeable effect on the vertical features. Indeed, the horizontal and vertical PSD plots are different, with the horizontal one showing a much clearer feature (iii). Figure 9g is a representative experimental STM image with its horizontal and vertical PSD plots shown in Figure 9h. The resemblance to the plots shown in Figure 9f is striking.

DISCUSSION

This work addressed a difficult experimental problem that has raised interest and controversy^{55,56} in the field of metal NPs: the identification of a self-organized pattern on the ligand shell of mixed-ligand-coated Au NPs from STM images. We have conceived the experiments with the aim of acquiring multiple images of the same sample at different locations with different

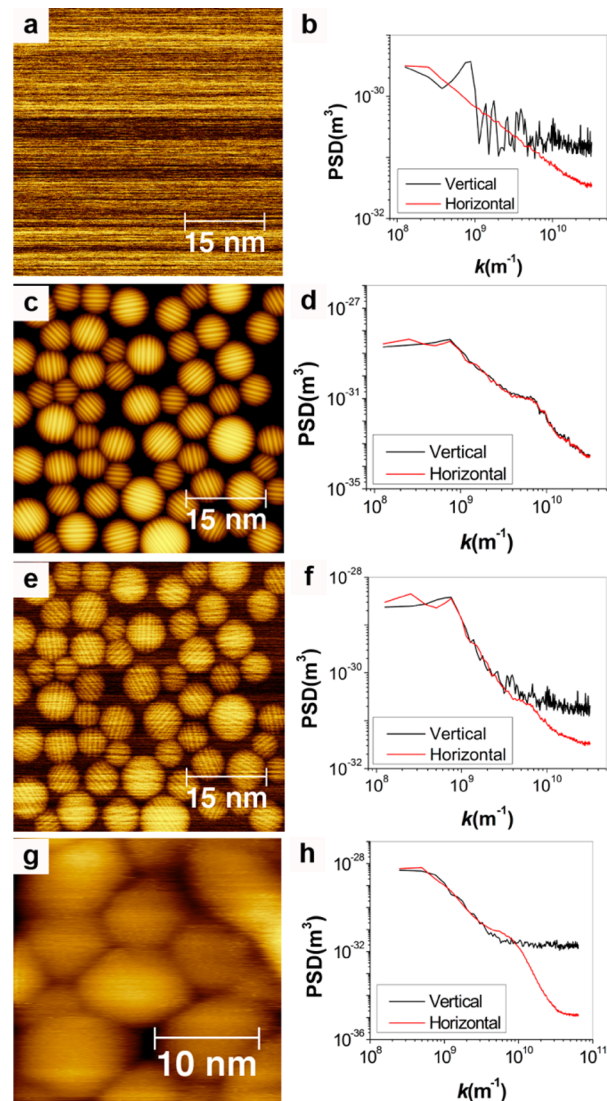


Figure 9. (a) Simulated image of the $1/f$ noise typically occurring in an STM image. (b) Vertical and horizontal PSD plots of the simulated image shown in a. (c) Image of particles with striped features on top; this is the same image shown in Figure 7a. (d) PSD plots of the image in c. (e) Image obtained as the sum of the images shown in a and c. (f) PSD plots of the image shown in e. (g) Representative experimental STM image of mixed-ligand nanoparticles with its PSD plots shown in h. The 2D FFT of this image is shown in Figure S7. The image was recorded at UdS with the following acquisition parameters: $L = 22.2 \text{ nm}$, $IS = 22.2 \text{ nm}$, $V_b = 200 \text{ mV}$, $I_t = 0.1 \text{ nA}$, $\nu = 10 \text{ Hz}$, and year 2013.

instruments and operators. We have applied a rigorous analysis method to compare the data acquired following criteria of robustness and operator independence. We have used the method to compare data across different laboratories and validate the data acquired earlier.^{29,35} Our goal was to identify the features in STM images that can be considered to be reproducible across samples (1:1 C4ol/C11ol and 2:1 OT/MPA), time (images compared here have been recorded from 2004 to 2013), instruments (Bruker Multimode Nanoscope IIIa, Agilent 5100 PicoLE, and LT-STM Omicron), piezoelectric scanners (for Bruker Multimodes E and A), and laboratories (MIT, EPFL, UG, UdS, and KUL).

Figure 1 provides qualitative evidence that similarities exist in the images acquired at the different laboratories. However,

visual inspection alone is not sufficient to assess unambiguously how similar the images are and whether the features observed can be quantitatively compared. The previously reported work^{29,35} has been based on an analysis carried out by operators extracting spatial information from a limited number of line profiles. On the one hand, real-space approaches use a small fraction of the information contained in the whole image. On the other hand, they may suffer from the subjectivity of the operator's choice.

To overcome these limitations, we have decided to rely on PSD analysis where the information contained in the image is analyzed without rejecting or choosing data ad hoc. The PSDs are built using data for the whole image, and they can be compared and averaged at all spatial frequencies. The PSD is the distribution of the different length scales (proportional to the inverse wave vector) in the image: the smaller the PSD intensity, the smaller the contribution of that spatial frequency to the squared fluctuation of the topography of the image. A maximum in the PSD (resonance) indicates the presence of a periodic modulation of the topography. A flat (white) spectrum shows that the spatial frequencies are all equally present in the signal. A power law decay indicates spatial correlations of the topographical features if the exponent is larger than 1.^{42,44,49} Within this framework, it is possible to trivialize the PSD as the probability that a certain spatial frequency occurs in the topography.

Typical PSD spectra of STM images of ligand-coated NPs are shown in Figure 2. Referring to the text in Results section, we find that plateau feature (i) is not as important per se, being limited by the scan length at lower frequencies. However, the presence of the plateau spanning several spatial frequencies is important in assessing that the process of background subtraction in the image has been done correctly. In the absence of large length scale motives, (i.e., features induced by the underlying substrate corrugation), the crossover frequency between the plateau and feature (ii) corresponds to the inverse average interparticle distance. In the case of Figure 2a, the crossover is not sharp but spans length scales ranging from below 10 nm (comparable to the average NP size) to 16.7 nm as a result of size polydispersity and the noncompact arrangement of particles in the images, generating the dispersion at the larger correlation length. Feature (ii) can be fit to power law decay, indicating that the smaller the length scale, the smaller the probability of finding it in the image. Such a trend is interrupted by the onset of feature (iii), indicating that the frequencies enveloped by feature (iii) occur in the image. The larger the departure of feature (iii) from the trend of the decaying tail of feature (ii), the more likely it is to identify such frequencies visually in the image. Feature (iii) occurs in the range of length scales that we ascribe to the presence of the spatial modulations on top of the NPs. We rationalize these observations by invoking the following arguments: (a) the shift of feature (iii) is correlated with the chemical composition of the NPs, as shown in Figure 2b; (b) as images change from showing crisp to blurry features, feature (iii) changes from a pronounced peak to a shoulder. Specifically, feature (iii) occurs in the range from 1.0 to 1.9 nm, and feature iv occurs in the range from 0.5 to 0.8 nm. As explained in the Results section, the lower limit of feature (iii) is what we can envision as the characteristic length scale present on the particles, with small effects of the windowing choice and consequently of the scan length. The upper limit of the length scale is set by the interplay between the orientational

distribution of the periodicity and the NP size distribution. The physical lower limit of feature iv is related to the molecular packing (e.g., Figure 5).

To quantify the characteristic length scales, we propose a phenomenological functional presented in eq 1 and applied to our data sets. The analytical form of the functional is inspired by the functional proposed in ref 57 to describe the height–height correlation function of a self-affine surface (i.e., a surface with spatially correlated topography fluctuations). The functional in ref 57 cannot be analytically transformed into a functional for fitting the PSD. It is clear that the functional in eq 1 has the proper form to reproduce well the features observed in the spectra and extract reliable values for the morphological parameters associated with the PSD features. Our attempts to fit the PSDs with a simpler functional (such as combination of Gaussian or Lorentzian functions) did not give satisfactory results.

We discuss now the choice of working with 1D PSD. We tested other possible schemes. Feature (iii) in radial PSD as well as in 2D PSD tends to be smeared out or practically absent in comparison to 1D PSD. This can be rationalized by looking at the spectral profiles along different directions (Figure 9). They look much alike, with the exception of the spectra in directions within $\sim 20^\circ$ of k_y , where the dominant $1/f$ noise contribution typical of scanning probe images blurs the features, as illustrated in Figure 9b, d.^{42,53} As a consequence, the choice of 1D PSD of the x axis (fast scan direction) is motivated by the minimization of the $1/f$ noise contribution from the y -axis scan. In 1D PSD, the images analyzed must exhibit a sufficient number of NPs to guarantee the ensemble averages. Such a choice might turn out not to be appropriate for those images at a small scan length where only one or a few NPs are present. Indeed, in this case, radial PSD might be preferred.

The PSD versus wave vector plots clearly show that feature (iii) is largely conserved across many images for the same mixed-ligand Au NP. Feature (iii) is not conserved when the PSDs are plotted against the time frequency obtained by rescaling according to eq 1. We conclude that feature (iii) represents a genuine spatial feature of the NPs on length scales smaller than the characteristic NP size. It is not due to feedback ringing (that would lead to a conserved feature in the time–frequency domain as shown clearly in Figure 3c for images acquired with very similar imaging parameters) or systematic artifacts (that would unlikely be conserved across laboratories, instruments, and operators). The shift in k_{c2} obtained from images of homiligand NPs indicates that feature (iii) is correlated to the ligand composition. We infer that feature (iii) is the fingerprint of the domain organization on ligand-coated NPs, representing a characteristic length scale distributed in the range of 1–1.9 nm for mixed-ligand NPs. It is important to stress that this characteristic length scale should be viewed as a correlation length rather than the periodicity of a highly ordered crystalline structure because NPs exhibit only short-range order.

It is now clear that the system under investigation has reproducible features spanning more than 1 order of magnitude of the spatial length scales. However, the amount of information acquired at the different spatial frequencies depends on the scan length. To acquire more information on the sub-NP length scale, we have acquired images whose size is comparable to that of single NPs. The results are shown in Figure 5a, where the headgroups of single molecules on the NP

are approximately aligned along stripes. The corresponding PSD, shown in Figure 5b, still exhibits a weak feature (iii) as the result of the occurrence of a few repeated stripes and a broad peak at ~ 0.5 nm consistent with feature iv. This PSD closely resembles the one by UG in Figure 2a acquired in UHV at low T . In both cases, a molecular packing whose length scale is close to 0.5 nm and domains with a length scale of 1 nm are imaged, resulting in the coalescence of features (iii) and (iv). We associate the 0.5 nm length scale with the distance between adjacent headgroups along the stripe. This value of the intermolecular spacing corresponds to the value observed in feature iv for homoligand NPs, which is consistent with the formation of a compact monolayer. The PSD of Figure 5b can be stitched together with the PSDs of images acquired on larger length scales, as shown in Figure 6. Our analysis across length scales teaches us that the system under investigation has morphological characteristics of a self-affine architecture across more than 1 order of magnitude of spatial length scales. In fact, molecular building blocks align along stripe-like domains whose correlation length is 0.5 nm along the stripe; the stripes form a self-organized structure on the NP with a 1 nm correlation length, and the NPs arrange into domains with a 10–16 nm correlation length. PSD stitching shows us a coherent picture at all investigated length scales of the distribution of spatial frequencies in the assemblies of mixed-ligand NPs.

The understanding that we gain from the PSD analysis is that the highest-frequency limit (corresponding to the smaller characteristic length scale) of feature (iii) for mixed-ligand NPs and feature iv for homoligand NPs establishes the correlation length. The broadening of the peak toward smaller frequencies (i.e., larger length scales) has to be ascribed to the NP orientation and possibly to curvature effects and their interplay with NP size.

To support our assignment of PSD features, we generated artificial images and extracted the PSD from them. In Figure 7a, an artificial image of an NP sample is shown. In Figure 7b, we show the cross section of the model used that is largely superimposed on the modulation observed in a real experimental line scan. In Figure 7c, we show that the PSD of the image in Figure 7a can be largely overlaid with the PSD of our experimental images, and in particular, feature (iii) is closely reproduced. Because no internal structure of the stripes has been generated, broad peak feature iv does not appear in the PSD. From this comparison, we conclude that our interpretation of the PSD is valid. We also use this comparison to confirm that the characteristic length scale on the NP corresponds quantitatively with the highest spatial frequency present in feature (iii). The PSDs of artificial images on different length scales have been used to assess the influence of aliasing.

We have also simulated nanoparticles imaged under unstable feedback loop conditions (Figure 8a). The latter were generated using the parameters and characteristics of the feedback loop when the gains and speed are high.⁵² In Figure 8c, we show a representative image of an NP sample taken with gains set sufficiently high to lead to feedback loop oscillations. There is a striking resemblance between the PSDs in Figure 8b of simulated images parametrized at different scan speeds and the experimental PSDs in Figure 8d of images acquired at different scan speeds. We notice that the experimental spectra in Figure 3b,c are more complex than those in Figure 8d, even though they are all from images that mostly contain feedback loop oscillations. The reason for the difference could be found

in the fact that whereas images analyzed in Figure 8 were generated with the sole scope of achieving and later analyzing feedback loop oscillations⁴⁰ images analyzed in Figure 4 were taken within the scope of investigating features on surfaces and only later were interpreted as containing feedback loop oscillations.²⁹ In both cases, there is a clear dependence of the PSD features on the scan speed. We conclude that the simulated PSDs account properly for the essential features and support our interpretation.

A final consideration, as well as an open question, concerns the origin of the feature (iii) for mixed-ligand NPs and feature iv for homoligand NPs. The NP in the STM junction is off-resonance with respect to the Fermi level of the tip and surface. In this regime, the STM current arises from the interplay of the hopping mechanism, where the electron spends a finite time on the NP, and tunneling. The ligand shell acts as an in-series capacitance that varies in space because of the modulation across the NP surface and in time because of the chain dynamics that can be also perturbed by the scanning tip. It turns out that the STM contrast within the NP cannot be explained by the local density of states on the Fermi level because the charge-transport mechanism in the STM junction is likely inelastic. Our hypothesis is that the broadening of feature (iii) might also be contributed by the presence of such effects, which prevent a sharp contrast of features as expected in SAMs on planar features. From an electrical analogue, this can be viewed as if the STM junction with the NP in the gap acts as an RC element. Its characteristic time scale will be modulated as the tip scans across different ligand positions. The mechanism of STM contrast through NPs needs to be investigated in depth. Here it suffices to remark that the feature broadening arises from positional disorder and size inhomogeneity in the case of features (i) and (ii), orientational disorder and spatial correlations in the case of features (iii) and (iv), and possibly the superposition of electronic effects in the charge transport across ligand-coated NPs.

CONCLUSIONS

We have shown a PSD-based analysis of STM images of ligand-protected Au NPs. We have assigned the PSD features that correlate with the characteristic length scales present on the NPs. The analysis of STM images has shown that mixed-ligand NPs exhibit a spatially correlated architecture with a periodicity of ~ 1 nm that is independent of the imaging conditions and can be reproduced in four different laboratories using three different STM microscopes. This PSD analysis also shows the same features on images that were previously analyzed with less-sophisticated methods. Importantly, the method allowed us to discriminate images that were strongly affected by noise in a data set containing genuine spatially correlated features. This would not be possible by direct inspection or analysis in real space. High-resolution images also show a smaller length scale of about 0.5 nm, which might be regarded as an intermolecular distance in the ligand shell and can also be found in homoligand NPs.

This work has further shown the complexity of the molecular organization on NPs. Because of its rapid and unambiguous interpretation of STM data, the PSD analysis has the potential to unveil unknown aspects of the static and dynamic organization of molecules on nanoparticles and curved surfaces. This analysis can be readily extended to scanning probe microscopy images of a variety of nanostructures such as nanoparticles, nanorods, and nanowires.⁵⁸

■ EXPERIMENTAL AND METHODS SECTION

Synthesis of Nanoparticles. The synthesis method described in ref 59 was modified to prepare Au nanoparticles coated with 11-mercaptop-1-undecanol (C11ol) and 4-mercaptop-1-butanol (C4ol). In a typical experiment, 0.25 mmol of chloro(triphenylphosphine) gold was dissolved in 20 mL of toluene/methanol 1:1 followed by the addition of a 0.25 mmol mixture of ligands C11ol/C4ol 1:1. The solution was constantly stirred for 10 min before the addition of 2.5 mmol of a borane morpholine complex dissolved in 20 mL of toluene/methanol 1:1. The solution was immediately refluxed at 105 °C and left to react for 1 h with constant stirring. The resulting colloidal solution was precipitated with methanol, and the solid product was cleaned with methanol and acetone in several cycles of redissolution and centrifugation. ¹H NMR spectra were recorded to ensure that the particles were clean (i.e., contained a minimum quantity of free ligands). Other NPs analyzed in this article are 1-octanethiol (OT)/mercaptopropionic acid (MPA) 2:1 and OT/MPA 30:1 first presented in 2004²⁹ and studied further in 2008.⁴⁰

Sample Preparation for STM. Au(111)-coated mica functionalized with a mixture of butanethiol and hexadecanedithiol was used as a substrate for STM experiments. To prepare a monolayer of Au nanoparticles, a KSV 2000 Langmuir–Blodgett trough (150 mm wide, 78 000 mm²) was used. A volume of 0.3 mL of Au nanoparticles (1 mg/mL) in toluene was placed dropwise on the water subphase. The barriers were closed at 10 mm/min. Once the solid phase was reached, the system was left to equilibrate, and the monolayer was transferred to the substrate in a parallel fashion (Langmuir–Schaefer deposition). The substrate was glued to a metal disk with double-sided carbon tape, on which another piece of carbon tape was placed to provide a current path from the substrate to the STM sample holder. The same sample was imaged at Ecole Polytechnique Fédérale de Lausanne (EPFL), Université de Genève (UG), Université de Strasbourg (UdS), and KU Leuven-University of Leuven (KUL) in this chronological order. At UG, the sample was subjected to a mild annealing (80 °C for 1 h) by means of a resistive heater in a vacuum chamber attached to the STM system (base pressure below 5 × 10⁻¹⁰ mbar). For the preparation of the OT/MPA 2:1 and OT/MPA 30:1 NPs, please refer to the original papers.²⁹

STM Imaging. Under ambient conditions, different STM microscopes at four different laboratories (MIT, EPFL, KUL, and UdS) were used to inspect the samples. At EPFL (and previously MIT), a Bruker Multimode equipped with an E-scanner and a Nanoscope IIIA controller was used. At KUL and UdS, the same type of microscope equipped with an A scanner at KUL and an A scanner connected to a low-current extended box at UdS was also used. In addition to a Bruker Multimode, an Agilent 5100 (PicoLE) microscope was also used at KUL. To make an STM tip, a Pt/Ir (80/20) wire was cleaned with a piece of dust-free Kimwipes paper soaked with ethanol, and the STM tip was freshly cut before use. Before we recorded images, a microscope was left scanning continuously for at least 12 h to improve the thermal stabilization and minimize the scanner hysteresis. Set-point currents are in the range from 50 pA to 2 nA, and bias voltages are in the range from 50 mV to 1 V. Integral gains are set between 0.3 and 1.5, and proportional gains are set between 0.5 and 1.5. Tip speeds are from 0.02 to 2 μm/s, and high-resolution images are recorded at the high end of the range. STM imaging under ultrahigh vacuum (UHV) and low temperature (LT) was carried out at UG using an LT-STM Omicron microscope operating at 77 K and a base pressure lower than 10⁻¹¹ mbar. In all recent images, the z dynamic range of the scanner used has been decreased to enhance the vertical resolution. This has been done adaptively, depending on the roughness of the scanned area. In particular, when a scan of a single nanoparticle was performed, the dynamic range was held to the minimum.

Image Analysis. Analysis was performed by the team of the corresponding author on STM images using Gwyddion open source software version 2.31 (<http://gwyddion.net>).⁶⁰ The power spectral density (PSD) has been used to investigate the topographic features observed in STM images of functionalized Au nanoparticles. The PSD is the norm-squared Fourier transform of topography $z(x, y)$ at

position (x, y) . PSD corresponds to the Fourier transform of autocorrelation function $\langle z(x, y) \cdot z(x', y') \rangle$.^{41,54} First we give the continuous definition, and then we translate it into a discrete form. The 2D PSD of a continuous function $z(x, y)$ is defined as

$$\text{PSD}_{2\text{D}}(k_x, k_y) = \left(\frac{1}{L} \right)^2 \left| \int_0^L dx e^{-ik_x x} \int_0^L dy e^{-ik_y y} z(x, y) \right|^2 \quad (3)$$

where the double integral is the 2D Fourier transform of topography $z(x, y)$ and wave vectors $k_x = 2\pi f_x$ and $k_y = 2\pi f_y$ are the coordinates of the reciprocal space, proportional to the spatial frequencies (inverse distances) f_x and f_y .

The 1D PSD used in this work is obtained as

$$\begin{aligned} \text{PSD}_{1\text{D}}(k_x) &= \frac{1}{2\pi} \int_{-\infty}^{+\infty} dk_y \text{PSD}_{2\text{D}}(k_x, k_y) \\ &= \frac{1}{2\pi} \left(\frac{1}{L} \right)^2 \int_{-\infty}^{+\infty} dk_y \left| \int_0^L dx e^{-ik_x x} \int_0^L dy e^{-ik_y y} z(x, y) \right|^2 \\ &= \frac{1}{2\pi} \left(\frac{1}{L} \right)^2 \int_{-\infty}^{+\infty} dk_y \int_0^L dx e^{-ik_x x} \int_0^L dy e^{-ik_y y} z(x, y) \\ &\quad \int_0^L dx' e^{ik_x x'} \int_0^L dy' e^{ik_y y'} z(x', y') \\ &= \left(\frac{1}{L} \right)^2 \int_0^L dx \int_0^L dy \int_0^L dx' e^{-ik_x(x-x')} \\ &\quad \int_0^L dy' \delta(y - y') z(x, y) z(x', y') \\ &= \left(\frac{1}{L} \right)^2 \int_0^L dx \int_0^L dx' e^{-ik_x(x-x')} \int_0^L dy z(x, y) z(x', y) \\ &= \left(\frac{1}{L} \right)^2 \int_0^L dy \left| \int_0^L dx' e^{-ik_x x} z(x, y) \right|^2 \end{aligned} \quad (4)$$

$$\text{PSD}_{1\text{D}}(k_x) = \frac{1}{L} \int_0^L dy |\tilde{z}(k_x, y)|^2 \quad (5)$$

Equation 5 is the mean on y of the norm-squared Fourier transform of the topography along x . Thus, $\text{PSD}_{1\text{D}}$ has a dimension of length cubed.

In STM images, topography z is defined at the nodes of the acquisition grid, viz. $z(x, y) = z(m\Delta, n\Delta)$, with $n, m = 0, 1, \dots, N - 1$, and $\Delta = L/N$ is the distance between two adjacent pixel (sampling interval). The discrete analogue of eq 5 becomes

$$\text{PSD}(k) = \frac{1}{N} \sum_{n=0}^{N-1} \frac{\Delta}{2\pi} \left| \sum_{m=0}^{N-1} z(m\Delta, n\Delta) \exp(-ikm\Delta) \right|^2 \quad (6)$$

Being equivalent to eq 4, eq 6 represents the integral over all k_y values of the 2D PSD. The analysis starts from raw data images acquired by the different microscopes. Squared images with $N \times N$ pixels (i.e., consisting of N lines of N pixels each) were used. Typically $N = 512$, but images with smaller number of lines were acquired or they were cropped from larger images without adding data points. We specify in the figure captions the number of pixels in each image or the number of frequencies in the PSD. Each image was treated as follows: the overall curvature was removed by subtraction of the best-fit paraboloid (second-order polynomial in 2D); then accidental scars due to loss of tip interaction or material drift were removed. The effect of these two operations on the PSD curve is illustrated in Figure S6. The (symmetrized) PSD in eq 6 is evaluated at $N/2$ evenly spaced values of wave vector k ranging from $2\pi/L$ to $N\pi/L$. In this work, we discard the zero-frequency value of the PSD because it is not relevant to the analysis. Radial PSDs (obtained by azimuthal averaging of the 2D PSD) and profiles drawn from 2D PSDs were consistently found to exhibit the same features as the 1D PSD. This should be noted because the radial PSD output by Gwyddion corresponds to the true radial PSD multiplied by the wave vector. Characteristic length scales of NPs reported in the text were evaluated by inverting the average frequencies extracted from the PSD features. The error cited for the characteristic length scales was estimated by the propagation of errors, starting from the standard deviation of the characteristic frequencies

identified. The analysis of all PSDs was carried out with IgorPro 6.22A (Wavemetrics, Lake Oswego, OR).

Simulated Images. Artificial images representing NPs were generated from a Matlab code that is able to create hemispheres with quasi-periodic features superimposed on them. To render the conceptual image as realistic as possible, we generated (a) a set of hemispheres with a size polydispersity similar to that of the C11ol/C4ol NP sample; (b) stripe features with slowly varying widths resembling the natural chemical fluctuations as well as edge effects present in our samples and images; and (c) stripe features with a randomly varying orientation. Finally, we account for tip convolution effects by applying a ball-rolling filter (10 nm) to the image. From these artificial images, the PSDs were estimated using the Gwyddion software as applied to experimental STM images.

Similar images were produced with the aim of simulating images generated by an excessive value of feedback gain and hence exhibiting feedback loop oscillations. These images were generated starting from the same artificial NP image used to represent striped nanoparticles as described above. The only difference was that all of the sub-NP features were removed, leaving bare hemispheres. Then, this image was used as an input in a Matlab code written to simulate the feedback loop of a simplified STM, according to eq 9 on page 36 of ref 52

$$I(s) = \frac{G(s) H(s)}{1 + G(s) H(s)} R(s)$$

where $G(s)$ is the function of the feedback control and $H(s)$ is the function of the mechanical response of the microscope, and eq 10 on page 37 of ref 52

$$H(s) = \frac{\alpha s + 1}{s^2 + \frac{\omega_0 s}{Q} + \omega_0^2}$$

where α is the time constant determining the phase of the response, ω_0 is the undamped resonance frequency, and Q is a quality factor. We set the parameters $\omega_0 = 2.6 \times 10^3$ rad/s and $Q = 20$; $\alpha = 2.6 \times 10^{-5}$ s. Because the purpose of our simulation was to model how noise scales with speed in a generic STM, we used the same parameters from ref 52 with no modification. To achieve feedback loop oscillations in the simulated image, we used large values for the parameters that represent integral and differential gains (4×10^{14} and 9×10^6 , respectively, and a proportional gain of 0). To simulate the dependence of the images on the speed of image acquisition, we kept all of the parameters constant and changed only the time step.

ASSOCIATED CONTENT

Supporting Information

Plots showing the fit to the PSD data presented. PSD of zero scan images in various laboratories. PSD plots from Figure 2 rescaled for the time frequency, for images of the same particles shown in Figure 5b, and for the same image before and after plane fit and scar removal. Representative power spectra (2D FFT). This material is available free of charge via the Internet at <http://pubs.acs.org>.

AUTHOR INFORMATION

Corresponding Author

*E-mail: fabio.biscarini@unimore.it.

Notes

The authors declare no competing financial interest.

ACKNOWLEDGMENTS

We thank Prof. Francesco Zerbetto (Alma Mater-Università di Bologna) for insightful comments. We thank Sébastien Haar for his technical support during the STM measurements in Strasbourg. We acknowledge partial support by EU Project FP7-NMP-2011-280772-2 “Implantable Organic Nano-Elec-

tronics” (I-ONE), EC-Marie-Curie ITN SUPERIOR (PITN-GA-2009-238177), the Agence Nationale de la Recherche through the LabEx project CSC and the International Center for Frontier Research in Chemistry (icFRC). K.M. and S.D.F. thank the Fund for Scientific Research - Flanders (FWO) for financial support.

REFERENCES

- (1) Sperling, R. A.; Rivera Gil, P.; Zhang, F.; Zanella, M.; Parak, W. J. Biological applications of gold nanoparticles. *Chem. Soc. Rev.* **2008**, *37*, 1896–1908.
- (2) Dreaden, E. C.; Alkilany, A. M.; Huang, X.; Murphy, C. J.; El-Sayed, M. A. The golden age: gold nanoparticles for biomedicine. *Chem. Soc. Rev.* **2012**, *41*, 2740–2779.
- (3) Daniel, M.-C.; Astruc, D. Gold nanoparticles: assembly, supramolecular chemistry, quantum-size-related properties, and applications toward biology, catalysis and nanotechnology. *Chem. Rev.* **2004**, *104*, 293–346.
- (4) Alibart, F.; Pleutin, S.; Guérin, D.; Novembre, C.; Lenfant, S.; Lmimouni, K.; Gamrat, C.; Vuillaume, D. An organic nanoparticle transistor behaving as a biological spiking synapse. *Adv. Funct. Mater.* **2010**, *20*, 330–337.
- (5) Du, J. J.; Jiang, L.; Shao, Q.; Liu, X. G.; Marks, R. S.; Ma, J.; Chen, X. D. Colorimetric detection of mercury ions based on plasmonic nanoparticles. *Small* **2013**, *9*, 1467–1481.
- (6) Klajn, R.; Stoddart, J. F.; Grzybowski, B. A. Nanoparticles functionalised with reversible molecular and supramolecular switches. *Chem. Soc. Rev.* **2010**, *39*, 2203–2237.
- (7) Tong, L.; Wei, Q. S.; Wei, A.; Cheng, J. X. Gold nanorods as contrast agents for biological imaging: optical properties, surface conjugation and photothermal effects. *Photochem. Photobiol.* **2009**, *85*, 21–32.
- (8) Ghosh, P.; Han, G.; De, M.; Kim, C. K.; Rotello, V. M. Gold nanoparticles in delivery applications. *Adv. Drug Delivery Rev.* **2008**, *60*, 1307–1315.
- (9) Ionita, P.; Volkov, A.; Jeschke, G.; Chechik, V. Lateral diffusion of thiol ligands on the surface of Au nanoparticles: an electron paramagnetic resonance study. *Anal. Chem.* **2007**, *80*, 95–106.
- (10) Lucarini, M.; Pasquato, L. ESR spectroscopy as a tool to investigate the properties of self-assembled monolayers protecting gold nanoparticles. *Nanoscale* **2010**, *2*, 668–676.
- (11) Gentilini, C.; Evangelista, F.; Rudolf, P.; Franchi, P.; Lucarini, M.; Pasquato, L. Water-soluble gold nanoparticles protected by fluorinated amphiphilic thiolates. *J. Am. Chem. Soc.* **2008**, *130*, 15678–15682.
- (12) Gentilini, C.; Franchi, P.; Mileo, E.; Polizzi, S.; Lucarini, M.; Pasquato, L. Formation of patches on 3D SAMs driven by thiols with immiscible chains observed by ESR spectroscopy. *Angew. Chem., Int. Ed.* **2009**, *48*, 3060–3064.
- (13) Lucarini, M.; Franchi, P.; Pedulli, G. F.; Gentilini, C.; Polizzi, S.; Pengo, P.; Scrimin, P.; Pasquato, L. Effect of core size on the partition of organic solutes in the monolayer of water-soluble nanoparticles: an ESR investigation. *J. Am. Chem. Soc.* **2005**, *127*, 16384–16385.
- (14) Possocco, P.; Gentilini, C.; Bidoggia, S.; Pace, A.; Franchi, P.; Lucarini, M.; Fermeglia, M.; Prich, S.; Pasquato, L. Self-organization of mixtures of fluorocarbon and hydrocarbon amphiphilic thiolates on the surface of gold nanoparticles. *ACS Nano* **2012**, *6*, 7243–7253.
- (15) Liu, X.; Yu, M.; Kim, H.; Mameli, M.; Stellacci, F. Determination of monolayer-protected gold nanoparticle ligand-shell morphology using NMR. *Nat. Commun.* **2012**, *3*, 1182.
- (16) Pradhan, S.; Brown, L. E.; Konopelski, J. P.; Chen, S. W. Janus nanoparticles: reaction dynamics and NOESY characterization. *J. Nanopart. Res.* **2009**, *11*, 1895–1903.
- (17) Pradhan, S.; Xu, L. P.; Chen, S. W. Janus nanoparticles by interfacial engineering. *Adv. Funct. Mater.* **2007**, *17*, 2385–2392.
- (18) Guarino, G.; Rastrelli, F.; Mancin, F. Mapping the nanoparticle-coating monolayer with NMR pseudocontact shifts. *Chem. Commun.* **2012**, *48*, 1523–1525.

- (19) Guarino, G.; Rastrelli, F.; Scrimin, P.; Mancin, F. Lanthanide-based NMR: a tool to investigate component distribution in mixed-monolayer-protected nanoparticles. *J. Am. Chem. Soc.* **2012**, *134*, 7200–7203.
- (20) Perrone, B.; Springhetti, S.; Ramadori, F.; Rastrelli, F.; Mancin, F. “NMR Chemosensing” using monolayer-protected nanoparticles as receptors. *J. Am. Chem. Soc.* **2013**, *135*, 11768–11771.
- (21) Ingram, R. S.; Hostetler, M. J.; Murray, R. W. Poly-hetero- ω -functionalized Alkanethiolate-Stabilized Gold Cluster Compounds. *J. Am. Chem. Soc.* **1997**, *119*, 9175–9178.
- (22) Centrone, A.; Hu, Y.; Jackson, A. M.; Zerbi, G.; Stellacci, F. Phase separation on mixed-monolayer-protected metal nanoparticles: a study by infrared spectroscopy and scanning tunneling microscopy. *Small* **2007**, *3*, 814–817.
- (23) Badia, A.; Cuccia, L.; Demers, L.; Morin, F.; Lennox, R. B. Structure and dynamics in alkanethiolate monolayers self-assembled on gold nanoparticles: A DSC, FT-IR, and deuterium NMR study. *J. Am. Chem. Soc.* **1997**, *119*, 2682–2692.
- (24) Sandhyarani, N.; Antony, M. P.; Selvam, G. P.; Pradeep, T. Melting of monolayer protected cluster superlattices. *J. Chem. Phys.* **2000**, *113*, 9794–9803.
- (25) Neyman, A.; Meshi, L.; Zeiri, L.; Weinstock, I. A. Direct imaging of the ligand monolayer on an anion-protected metal nanoparticle through cryogenic trapping of its solution-state structure. *J. Am. Chem. Soc.* **2008**, *130*, 16480–16481.
- (26) Wang, Y. F.; Neyman, A.; Arkhangelsky, E.; Gitis, V.; Meshi, L.; Weinstock, I. A. Self-assembly and structure of directly imaged inorganic-anion monolayers on a gold nanoparticle. *J. Am. Chem. Soc.* **2009**, *131*, 17412–17422.
- (27) Yang, J. A.; Murphy, C. J. Evidence for patchy lipid layers on gold nanoparticle surfaces. *Langmuir* **2012**, *28*, 5404–5416.
- (28) Gusev, A. O.; Taleb, A.; Silly, F.; Charra, F.; Pilani, M. P. Inhomogeneous photon emission properties of self-assembled metallic nanocrystals. *Adv. Mater.* **2000**, *12*, 1583–1587.
- (29) Jackson, A. M.; Myerson, J. W.; Stellacci, F. Spontaneous assembly of subnanometre-ordered domains in the ligand shell of monolayer-protected nanoparticles. *Nat. Mater.* **2004**, *3*, 330–336.
- (30) Kuna, J. J.; Voitchovsky, K.; Singh, C.; Jiang, H.; Mwenifumbo, S.; Ghorai, P. K.; Stevens, M. M.; Glotzer, S. C.; Stellacci, F. The effect of nanometre-scale structure on interfacial energy. *Nat. Mater.* **2009**, *8*, 837–842.
- (31) Singh, C.; Ghorai, P. K.; Horsch, M. A.; Jackson, A. M.; Larson, R. G.; Stellacci, F.; Glotzer, S. C. Entropy-mediated patterning of surfactant-coated nanoparticles and surfaces. *Phys. Rev. Lett.* **2007**, *99*.
- (32) Stranick, S. J.; Atre, S. V.; Parikh, A. N.; Wood, M. C.; Allara, D. L.; Winograd, N.; Weiss, P. S. Nanometer-scale phase separation in mixed composition self-assembled monolayers. *Nanotechnology* **1996**, *7*, 438.
- (33) Stranick, S. J.; Kamna, M. M.; Krom, K. R.; Parikh, A. N.; Allara, D. L.; Weiss, P. S. Scanning tunneling microscopy studies of self-assembled monolayers of alkanethiols on gold. *J. Vac. Sci. Technol., B* **1994**, *12*, 2004–2007.
- (34) Stranick, S. J.; Parikh, A. N.; Tao, Y. T.; Allara, D. L.; Weiss, P. S. Phase separation of mixed-composition self-assembled monolayers into nanometer scale molecular domains. *J. Phys. Chem.* **1994**, *98*, 7636–7646.
- (35) Jackson, A. M.; Hu, Y.; Silva, P. J.; Stellacci, F. From homiligand- to mixed-ligand-monolayer-protected metal nanoparticles: A scanning tunneling microscopy investigation. *J. Am. Chem. Soc.* **2006**, *128*, 11135–11149.
- (36) Ong, Q. K.; Reguera, J.; Silva, P. J.; Moglianetti, M.; Harkness, K.; Longobardi, M.; Mali, K. S.; Renner, C.; Feyter, S. D.; Stellacci, F. High-resolution scanning tunneling microscopy characterization of mixed monolayer protected gold nanoparticles. *ACS Nano* **2013**, DOI: 10.1021/nn402414b.
- (37) Moglianetti, M.; Ong, Q. K.; Reguera, J.; Harkness, K.; Mameli, M.; Grillo, I.; Radulescu, A.; Jud, C.; Kohlbrecher, J.; Svergun, D.; Stellacci, F. Scanning tunneling microscopy and small angle neutron scattering study of mixed monolayer protected gold nanoparticles in organic solvents. Submitted for publication, 2013.
- (38) Egorov, S. A. Microphase separation of mixed polymer brushes physisorbed on cylindrical surfaces. *Soft Matter* **2012**, *8*, 3971–3979.
- (39) Miller, W. L.; Bozorgui, B.; Klymko, K.; Cacciuto, A. Free energy of alternating two-component polymer brushes on cylindrical templates. *J. Chem. Phys.* **2011**, *135*, 244902–244905.
- (40) Hu, Y.; Wunsch, B. H.; Sahni, S.; Stellacci, F. Statistical analysis of scanning tunneling microscopy images of ‘striped’ mixed monolayer protected gold nanoparticles. *J. Scanning Probe Microsc.* **2009**, *4*, 24–35.
- (41) Press, W. H.; Teukolsky, S. A.; Vetterling, W. T.; Flannery, B. P. *Numerical Recipes in C: The Art of Scientific Computing*; Cambridge University Press: New York, 2007.
- (42) Dumas, P.; Bouffakreddine, B.; Amra, C.; Vatel, O.; Andre, E.; Galindo, R.; Salvan, F. Quantitative microroughness analysis down to the nanometer scale. *Europhys. Lett.* **1993**, *22*, 717.
- (43) Nečas, D.; Klapetek, P. One-dimensional autocorrelation and power spectrum density functions of irregular regions. *Ultramicroscopy* **2013**, *124*, 13–19.
- (44) Biscarini, F.; Samori, P.; Greco, O.; Zamboni, R. Scaling behavior of anisotropic organic thin films grown in high vacuum. *Phys. Rev. Lett.* **1997**, *78*, 2389–2392.
- (45) Calò, A.; Stolar, P.; Bystranova, E.; Valle, F.; Biscarini, F. Measurement of DNA morphological parameters at highly entangled regime on surfaces. *J. Phys. Chem. B* **2009**, *113*, 4987–4990.
- (46) Dinelli, F.; Murgia, M.; Levy, P.; Cavallini, M.; Biscarini, F.; de Leeuw, D. M. Spatially correlated charge transport in organic thin film transistors. *Phys. Rev. Lett.* **2004**, *92*, 116802.
- (47) Valle, F.; Bianchi, M.; Tortorella, S.; Pierini, G.; Biscarini, F.; D'Eliac, M. Nanotechnology for forensic sciences: analysis of PDMS replica of the case head of spent cartridges by optical microscopy, SEM and AFM for the ballistic identification of individual characteristic features of firearms. *Forensic Sci. Int.* **2012**, *222*, 288–297.
- (48) Munoz, A. G.; Vela, M. E.; Salvarezza, R. C. Complex surface dynamics during anodic dissolution of Ni. *Langmuir* **2005**, *21*, 9238–9245.
- (49) Krim, J.; Palasantzas, G. Experimental-observations of self-affine scaling and kinetic roughening at submicron lengthscales. *Int. J. Mod. Phys. B* **1995**, *9*, 599–632.
- (50) Family, F.; Vicsek, T. Scaling of the active zone in the Eden process on percolation networks and the ballistic deposition model. *J. Phys. A: Math. Gen.* **1985**, *18*, L75.
- (51) Butt, H. J.; Guckenberger, R.; Rabe, J. P. Quantitative scanning tunneling microscopy and scanning force microscopy of organic materials. *Ultramicroscopy* **1992**, *46*, 375–393.
- (52) Stroscio, J.; Kaiser, W. *Scanning Tunneling Microscopy*; Academic Press: Boston, 1993.
- (53) Pancorbo, M.; Anguiano, E.; Aguilar, M. Fractal characterization by frequency analysis III. Effect of noise. *J. Microsc.* **1994**, *176*, 54–62.
- (54) Fang, S. J.; Haplepete, S.; Chen, W.; Helms, C. R.; Edwards, H. Analyzing atomic force microscopy images using spectral methods. *J. Appl. Phys.* **1997**, *82*, 5891–5898.
- (55) Cesbron, Y.; Shaw, C. P.; Birchall, J. P.; Free, P.; Levy, R. Stripy nanoparticles revisited. *Small* **2012**, *8*, 3714–3719.
- (56) Yu, M.; Stellacci, F. Response to “striped nanoparticles revisited”. *Small* **2012**, *8*, 3720–3726.
- (57) Weber, W.; Lengeler, B. Diffuse scattering of hard X rays from rough surfaces. *Phys. Rev. B* **1992**, *46*, 7953–7956.
- (58) Henry, C. R. Morphology of supported nanoparticles. *Prog. Surf. Sci.* **2005**, *80*, 92–116.
- (59) Zheng, N.; Fan, J.; Stucky, G. D. One-step one-phase synthesis of monodisperse noble-metallic nanoparticles and their colloidal crystals. *J. Am. Chem. Soc.* **2006**, *128*, 6550–6551.
- (60) Nečas, D.; Klapetek, P. Gwyddion: an open-source software for SPM data analysis. *Cent. Eur. J. Phys.* **2012**, *10*, 181–188.